energies

MDPI

Article

Influence of Polarity Reversal Period and Temperature Gradient on Space Charge Evolution and Electric Field Distribution in HVDC Extruded Cable

Yifan Zhou [1,2,*], Bo Gao [1,2], Wei Wang [1,2] and Ke Song [1,2]

[1] Beijing Key Laboratory of High Voltage & Electromagnetic Compatibility, North China Electric Power University, Beijing 102206, China; gaobo0510@ncepu.edu.cn (B.G.); wwei@ncepu.edu.cn (W.W.); songke0513@ncepu.edu.cn (K.S.)

[2] State Key Laboratory of Alternate Electrical Power System with Renewable Energy Sources, North China Electric Power University, Beijing 102206, China

* Correspondence: yfzhou@ncepu.edu.cn

Abstract: During the operation of HVDC extruded cables, voltage polarity reversal (VPR) is considered one of the most severe conditions for cable insulation. In this paper, a bipolar charge transport model developed for cylindrical geometry is improved by introducing ionic carriers from impurity dissociation for the simulation of space charge and electric field in an HVDC extruded cable with thick polymeric insulation under VPR, and the construction of the geometric model is based on a practical 160 kV DC polymeric cable. The influence of polarity reversal period (PRP) and temperature gradient (TG), formed by the load current flowing through the conductor, on the space charge evolution and the electric field distribution are investigated. The mechanisms of the charge dynamics and the field distortion affected by the PRP and the TG are also discussed. The results show that under TG, the maximum transient field appears near the interface between the conductor shield and insulation in the early stage of complete VPR. In addition, the longer the PRP, the more serious the maximum transient field distortion. Moreover, an increase in TG intensifies the maximum field distortion under steady and transient states due to the enhancement of heterocharge accumulation.

Keywords: HVDC extruded cable; polymeric insulation; space charge; polarity reversal period; temperature gradient; charge transport; ionic charge

Citation: Zhou, Y.; Gao, B.; Wang, W.; Song, K. Influence of Polarity Reversal Period and Temperature Gradient on Space Charge Evolution and Electric Field Distribution in HVDC Extruded Cable. *Energies* **2022**, *15*, 985. https://doi.org/10.3390/en15030985

Academic Editor: Zheng Xu

Received: 9 November 2021
Accepted: 25 January 2022
Published: 28 January 2022

1. Introduction

High-voltage direct-current (HVDC) transmission technology is widely used in long-distance and large-capacity transmission and regional power grids interconnection [1]. As a key piece of equipment in HVDC transmission system, the HVDC extruded cable provides significant advantages in terms of large transmission capacity and long-term reliability [2].

One of the primary factors restricting the development of polymeric insulation for HVDC extruded cables is the space charge accumulation, which distorts the local electric field, accelerates insulation aging and even causes insulation breakdown [3–5]. The space charge accumulation poses a greater threat.

In the line-commutated-converter (LCC) HVDC system, power flow reversal is implemented by voltage polarity reversal (VPR). With the polarity reversal (PR) process, the cable insulation is subjected to a high transient field caused by the superimposition of the applied DC field and the distorted field induced by space charge. This is a severe challenge to polymeric insulation for HVDC extruded cables. The polarity reversal period (PRP) is a crucial component affecting the VPR process. According to the CIGRE technical brochure in [6], the recommended PRP is within 2 min. Especially, a shorter PRP under emergency power control condition can be required to provide emergency support, which can accomplish the VPR within a few seconds [7]. In addition, a radially distributed temperature

gradient (TG) across the cable insulation is formed by the Joule heat originating from the load current flowing through the conductor. Hence, the effect of TG in the cable insulation is also a non-ignorable factor during the VPR. With the expansion of transmission distance, the increase in voltage level and the enlargement of transmission capacity require a stable operation of the HVDC extruded cable, with a high current-carrying capacity. In this case, the influence of the TG formed by high load current on the charge dynamics and the field distribution under the VPR becomes necessary for a reliable assessment of the cable insulation performance.

The space charge evolution in insulating materials under VPR and its influencing factors have been recently investigated on the basis of experimental measurement methods. Wu et al. [8] analyzed the influence of PRP on space charge and transient field in low density polyethylene (LDPE) film under TG. They found that the decrease in PRP results in decreasing the maximum transient field under TG. Tu et al. [9] evaluated the influence of VPR on the space charge characteristics in a Nano-CB/LDPE composite film using the pulsed electro-acoustic (PEA) method. They demonstrate that the composite film containing 0.03 wt.% CB nanoparticles shows a better effect in suppressing the charge accumulation after the VPR. Tanaka et al. [10] found that a large amount of packet-like charge accumulates in normal cross-linked polyethylene (XLPE) used in the cable insulation after the VPR, and the local electric field is significantly enhanced by the space charge accumulation. Du et al. [11] researched the influence of VPR on the distribution of space charge and the properties of breakdown in XLPE/graphene oxide (GO) nanocomposites. They demonstrate that space charge injection and accumulation show polarity dependence under the VPR, and the increase in the pre-applied hetero-polarity field decreases the breakdown strength in the XLPE film-type samples.

However, these studies focus on the thin film-type sample, which cannot directly extrapolate the HVDC extruded cable. The polymeric insulation for HVDC extruded cable is not only related to the insulation material characteristics, but also connected with the coaxial structure, leading to a field gradient inside the insulation. Moreover, the semi-conductive shielding layer cannot be ignored in the HVDC extruded cable.

Dissado et al. [12] investigated the space charge evolution in an actual XLPE cable under DC field during VPR, using the PEA technique. However, the investigation of the influence of the TG on the charge distribution only aims at the condition under an applied voltage with a steady unipolarity. Therefore, this research lacks the charge evolution and the transient field distribution affected by the TG under the VPR in the XLPE cable.

The PEA measurement technique in a full-size HVDC cable is an effective method to recognize the space charge characteristics. However, this technology still possesses some limitations. Firstly, the full-size cable test is required to stripe part of the outer shields of the cable (e.g., water blocking layer and metal sheath). This affects the assessment of the cable's overall performance. Furthermore, several technique difficulties still need to be solved in order to improve the spatial resolution and the measurement sensitivity of the PEA system, especially for the space charge measurement in an HVDC extruded cable with thick polymeric insulation. Hence, numerical simulation based on polymer charge transport theory gradually becomes a supplementary method to effectively characterize the charge accumulation and the field distribution. A bipolar charge transport (BCT) model proposed by Alison et al. [13] is widely used for simulation of the space charge behavior in the film-type sample. Le Roy et al. [14] extended the BCT model used in the film-type sample to cable geometry, taking into account a steady TG across the insulation. Chen et al. [15] improved the BCT model developed for cable geometry, on the basis of the thermal transient effects. However, the current BCT model applied to cable geometry still retains some limitations in the following expressions. (i) The cable geometry used in the model is simplified: it only consists of the conductor and the insulation layer, which is different from the structure of an actual HVDC extruded cable. (ii) The carriers' diffusion in the insulation under the TG is neglected. (iii) The charge generation in the model is limited, with only electron and hole being injected from electrodes. Impurities, such as

crosslinking by-products and antioxidants [16,17], are unavoidable in the preparation process of polymeric insulation used in the HVDC extruded cable. The ionic carriers from the dissociation of impurities existing in polymeric insulation is another important source of space charge. It has been reported in [18–22] that the heterocharge formation is related to the dissociation of impurities. However, rare research on the space charge modelling in the HVDC extruded cable considers the contribution from the dissociation of impurities.

To date, the existing simulations based on the BCT model mainly focus on the insulation under an applied DC voltage with a unipolarity, while little attention has been paid to the effect of VPR on the charge accumulation and the field distribution, especially during the operation of a practical HVDC extruded cable. To the best of our knowledge, research about the influence of PRP on the charge evolution and the field distortion in the cable insulation are still lacking at present. In addition, the effect of TG formed by a high load current on the charge dynamics and the field distortion under the VPR in the cable insulation still requires further in-depth analysis. The mechanism whereby the PPR and the TG influence the charge dynamics and the field distortion in the cable insulation has not yet been elucidated.

In this paper, the ionic carriers from the impurity dissociation are introduced in the BCT model developed for cylindrical geometry. The remainder of this paper is organized as follows. Section 2 details the simulation method. More precisely, Section 2.1 presents the principle of the improved model with the BCT model and ion charge transport (ICT) model. The geometric model, initial conditions and boundary conditions used in the simulation are provided in Sections 2.2 and 2.3. On the basis of the improved model, the influence of PRP and TG on the evolution of space charge and the distribution of electric field are investigated in Section 3. The mechanisms by which the PRP and the TG influence the charge dynamics and the field distortion are discussed in Section 4. Finally, conclusions are drawn in Section 5.

2. Simulation Method

2.1. Improved Charge Transport Model for Cylindrical Geometry

The simulation based on the improved charge transport model for cylindrical geometry is implemented by using the finite element method (FEM), and the flow chart of the simulation implementation is shown in Figure 1.

2.1.1. BCT Model for Cylindrical Geometry

The BCT model consists of the process of charge injection, transport, trapping, de-trapping, recombination and extraction. Electrons and holes are respectively denoted by subscripts e and h, the coefficients of trapping and de-trapping are respectively represented by B_e/B_h and D_e/D_h, $S_{0\sim3}$ denotes the recombination coefficients of the trapped electrons (et)/trapped holes (ht), mobile electrons ((eμ)/ht, et/mobile holes (hμ)) and eμ/hμ.

When an applied DC electric field exceeds the threshold value for charge injection, the charge injection from both electrodes can be described by the Schottky law [15]:

$$\begin{cases} j_h(r_{in},t) = AT^2(r)\exp\left(-\frac{w_{ih}}{k_BT(r)}\right)\exp\left(\frac{e}{k_BT(r)}\sqrt{\frac{eE(r_{in},t)}{4\pi\varepsilon_0\varepsilon_r}}\right) \\ j_e(r_{out},t) = AT^2(r)\exp\left(-\frac{w_{ie}}{k_BT(r)}\right)\exp\left(\frac{e}{k_BT(r)}\sqrt{\frac{eE(r_{out},t)}{4\pi\varepsilon_0\varepsilon_r}}\right) \end{cases} \quad (1)$$

where $j_h(r_{in},t)$ and $j_e(r_{out},t)$ are respectively the injection current densities for holes and electrons, A is the Richardson constant, $T(r)$ denotes the temperature at the radius r of the insulation layer, w_{ih} and w_{ie} respectively represent the injection barriers for holes and electrons, k_B is the Boltzmann constant, $E(r_{in},t)$ and $E(r_{out},t)$ are respectively the electric fields at the radius of r_{in} and r_{out}.

The fundamental equations governing the charge dynamics in cylindrical coordinates are expressed as:

$$\begin{cases} \frac{\partial n_{\mathrm{a}}(r,t)}{\partial t} + \frac{1}{r}\frac{\partial (j_{\mathrm{a}} \cdot r)}{\partial r} = s_{\mathrm{a}}(r,t) \\ j_{\mathrm{a}\mu}(r,t) = \mu_{\mathrm{a}\mu}(r,t) n_{\mathrm{a}\mu}(r,t) E(r,t) - D_{\mathrm{f}} \frac{d n_{\mathrm{a}\mu}(r,t)}{dr} \\ \frac{\partial^2 V(r,t)}{\partial r^2} + \frac{1}{r}\frac{\partial V(r,t)}{\partial r} = -\frac{\rho(r,t)}{\varepsilon_0 \varepsilon_r} \end{cases} \tag{2}$$

where n_{a} denotes the carrier density, subscript a represents the density of different carriers, $j_{\mathrm{a}\mu}$ is the current density, $\mu_{\mathrm{a}}(r,t)$ denotes the mobility of the mobile carriers, V is the applied voltage, $\rho(r,t)$ represents the net charge density, and D_{f} refers to the diffusion coefficient which describes the diffusion movement of the mobile carriers. D_{f} follows the Einstein relation, and is given by:

$$D_{\mathrm{f}}(r,t) = \mu_{\mathrm{a}}(r,t) \cdot \frac{k_B T(r)}{e} \tag{3}$$

The charge transport between the shallow traps is characterized by the hopping mechanism, $\mu_{\mathrm{a}}(r,t)$ as a function of the field gradient and the TG dependency [23] is defined by:

$$\mu_{\mathrm{e,h}}(r,t) = \frac{2\lambda v}{E(r,t)} \exp\left(\frac{-w_{\mathrm{e}\mu,\mathrm{h}\mu}}{k_B T(r)}\right) \sinh\left(\frac{eE(r,t)\lambda}{2k_B T(r)}\right) \tag{4}$$

where λ denotes the distance between traps, $w_{\mu\mathrm{e}}$ and $w_{\mu\mathrm{h}}$ respectively represent the hopping barrier heights for electrons and holes, v is the attempt to escape frequency ($v = k_{\mathrm{B}} T(r)/h$), where h denotes the Planck constant.

In (2), $s_{\mathrm{a}}(r,t)$ is the source term for the bipolar carriers which indicates the changes of the local charge density caused by the non-conduction process, expressed as [24]:

$$\begin{cases} s_{\mathrm{e}\mu} = \frac{\partial n_{\mathrm{e}\mu}}{\partial t} = -S_1 n_{\mathrm{ht}} n_{\mathrm{e}\mu} - S_3 n_{\mathrm{h}\mu} n_{\mathrm{e}\mu} - B_{\mathrm{e}} n_{\mathrm{e}\mu}\left(1 - \frac{n_{\mathrm{et}}}{n_{\mathrm{oet}}}\right) + D_{\mathrm{e}} n_{\mathrm{et}} \\ s_{\mathrm{h}\mu} = \frac{\partial n_{\mathrm{h}\mu}}{\partial t} = -S_2 n_{\mathrm{et}} n_{\mathrm{h}\mu} - S_3 n_{\mathrm{h}\mu} n_{\mathrm{e}\mu} - B_{\mathrm{h}} n_{\mathrm{h}\mu}\left(1 - \frac{n_{\mathrm{ht}}}{n_{\mathrm{oht}}}\right) + D_{\mathrm{h}} n_{\mathrm{ht}} \\ s_{\mathrm{et}} = \frac{\partial n_{\mathrm{et}}}{\partial t} = -S_2 n_{\mathrm{h}\mu} n_{\mathrm{et}} - S_0 n_{\mathrm{ht}} n_{\mathrm{et}} + B_{\mathrm{e}} n_{\mathrm{e}\mu}\left(1 - \frac{n_{\mathrm{et}}}{n_{\mathrm{oet}}}\right) - D_{\mathrm{e}} n_{\mathrm{et}} \\ s_{\mathrm{ht}} = \frac{\partial n_{\mathrm{ht}}}{\partial t} = -S_1 n_{\mathrm{ht}} n_{\mathrm{e}\mu} - S_0 n_{\mathrm{ht}} n_{\mathrm{et}} + B_{\mathrm{h}} n_{\mathrm{h}\mu}\left(1 - \frac{n_{\mathrm{ht}}}{n_{\mathrm{oht}}}\right) - D_{\mathrm{h}} n_{\mathrm{ht}} \end{cases} \tag{5}$$

where n_{oet} and n_{oht} respectively represent the trap densities of electrons and holes, D_{e} and D_{h} are given by:

$$\begin{cases} D_{\mathrm{e}}(r,t) = v \exp\left(\frac{-\psi_{\mathrm{et}}}{k_B T(r)}\right) \\ D_{\mathrm{h}}(r,t) = v \exp\left(\frac{-\psi_{\mathrm{ht}}}{k_B T(r)}\right) \end{cases} \tag{6}$$

where ψ_{et} and ψ_{ht} represent the de-trapping barrier heights for n_{et} and n_{ht}, respectively.

The mobile carriers are extracted at the counter electrodes, with extraction fluxes j_e and j_{h}, given by [25]:

$$\begin{cases} j_{\mathrm{e}}(r,t) = C_{\mathrm{e}} \mu_{\mathrm{e}}(r,t) n_{\mathrm{e}\mu}(r,t) E(r,t) \\ j_{\mathrm{h}}(0,t) = C_{\mathrm{h}} \mu_{\mathrm{h}}(0,t) n_{\mathrm{h}\mu}(0,t) E(0,t) \end{cases} \tag{7}$$

where C_{e} and C_{h} respectively denote the extraction coefficients, reducing from being immediate ($C_{\mathrm{e/h}} = 1$) to fully blocking ($C_{\mathrm{e/h}} = 0$).

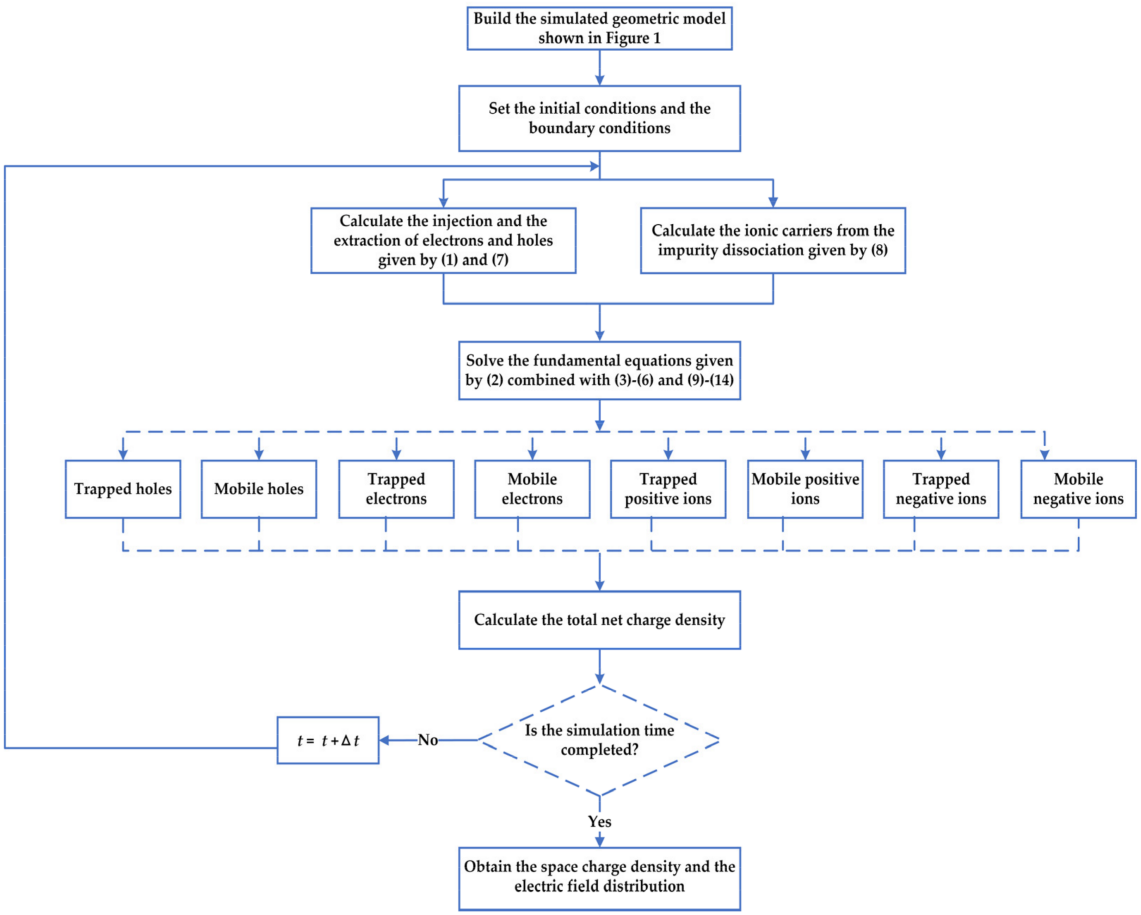

Figure 1. The flow chart of the simulation implementation.

2.1.2. ICT Model for the Cylindrical Geometry

The space charge also originates from the impurity dissociation. To simplify the type of impurities in the polymeric insulation for HVDC extruded cable, it is assumed that the impurity molecules can be thermally activated and dissociated into positive and negative ions. The dissociation coefficient is expressed as [26]:

$$D_{\mathrm{d}}(r,t) = v \exp\left(\frac{-\psi_{\mathrm{dis}}}{k_B T(r)}\right) \tag{8}$$

where ψ_{dis} is the dissociation barrier of ions.

The ionic carrier transport is described by the hopping barrier model, i.e., under the applied field, the generated ions are transported towards the counter electrodes by overcoming a barrier. The mobility of ionic carriers is defined by [26]:

$$\mu_{\mathrm{i}}(r,t) = \frac{\delta_{\mathrm{i}} v}{6E(r,t)} \exp\left(\frac{-w_{\mathrm{ti}}}{k_B T(r)}\right)\left[\exp\left(\frac{w_{\mathrm{i}}}{k_B T(r)}\right) - \exp\left(\frac{-w_{\mathrm{i}}}{k_B T(r)}\right)\right] \tag{9}$$

where subscript i denotes the type of ionic carriers, i.e., mobile positive ions (pμ) and negative ions (nμ), δ_{i} represents the average migration distance, w_{ti} is the migration barrier, w_{i} represents the decrease of w_{ti} under the applied field, given by:

$$w_{\mathrm{i}} = \frac{1}{2}\delta_{\mathrm{i}} eE(r,t) \tag{10}$$

The fundamental equations for the ionic charge dynamics in the cylindrical coordinates can also be governed by (2). Hence, the total net charge density $\rho(r,t)$ is composed of eight

types of carriers, containing mobile and trapped carriers for electrons, holes, positive ions and negative ions. In (2), the source term $s_a(r,t)$ is expressed as:

$$\begin{cases} s_{n\mu} = \frac{\partial n_{n\mu}}{\partial t} = -\xi_1 n_{pt} n_{n\mu} - \xi_3 n_{p\mu} n_{n\mu} - B_n n_{n\mu}(1 - \frac{n_{nt}}{n_{ont}}) + D_n n_{nt} + D_d N_0{}' \\ s_{p\mu} = \frac{\partial n_{p\mu}}{\partial t} = -\xi_2 n_{nt} n_{p\mu} - \xi_3 n_{p\mu} n_{n\mu} - B_p n_{p\mu}(1 - \frac{n_{pt}}{n_{opt}}) + D_p n_{pt} + D_d N_0{}' \\ s_{nt} = \frac{\partial n_{nt}}{\partial t} = -\xi_2 n_{p\mu} n_{nt} - \xi_0 n_{pt} n_{nt} + B_n n_{n\mu}(1 - \frac{n_{nt}}{n_{ont}}) - D_n n_{nt} \\ s_{pt} = \frac{\partial n_{pt}}{\partial t} = -\xi_1 n_{pt} n_{n\mu} - \xi_0 n_{pt} n_{nt} + B_p n_{p\mu}(1 - \frac{n_{pt}}{n_{opt}}) - D_p n_{pt} \end{cases} \quad (11)$$

where $\xi_{0\sim3}$ respectively denotes the recombination coefficients of the trapped positive ions (pt)/trapped negative ions (nt), mobile negative ions (nμ)/pt, nt/mobile positive ions (pμ), and pμ/nμ, n_{opt} and n_{ont} respectively represent the trap densities of the positive and negative ions, B_p and B_n are the trapping coefficients for positive and negative ions. The de-trapping coefficients D_p and D_n are expressed as:

$$\begin{cases} D_p(r,t) = v \exp\left(\frac{-\psi_{pt}}{k_B T(r)}\right) \\ D_n(r,t) = v \exp\left(\frac{-\psi_{nt}}{k_B T(r)}\right) \end{cases} \quad (12)$$

where ψ_{pt} and ψ_{nt} are respectively the de-trapping barrier heights for the trapped positive and negative ions n_{pt} and n_{nt}. $N_{0'}$ denotes the concentration of residual impurities, given by:

$$N_0{}' = N_0 - (S_\xi - D_d N_0) \quad (13)$$

where N_0 is the concentration of impurities and S_ξ represents the concentration of impurities formed by recombination per unit time:

$$S_\xi = \xi_0 n_{pt} n_{nt} + \xi_1 n_{pt} n_{n\mu} + \xi_2 n_{p\mu} n_{nt} + \xi_3 n_{p\mu} n_{n\mu} \quad (14)$$

The mobile ionic carriers reaching the counter electrode are fully blocked at the counter electrodes, i.e., the current densities of extracted ionic carriers on both electrodes are set to zero.

The simulation parameters are selected on the basis of the guidance from existing research [23,24,26]. They are provided in Table 1.

Table 1. The simulation parameters.

BCT Model		
Parameter	**Value**	**Units**
w_{ie}	1.3	eV
w_{ih}	1.27	eV
λ	3×10^{-8}	m
$w_{\mu e}$	0.62	eV
$w_{\mu h}$	0.68	eV
B_e	0.06	s^{-1}
B_h	0.12	s^{-1}
n_{0et}	100	C/m^3
n_{0ht}	100	C/m^3
ψ_{et}	0.9	eV
ψ_{ht}	0.95	eV
S_0,S_1,S_2	4×10^{-3}	m^{-3} C/s
S_3	0	m^{-3} C/s
C_e,C_h	0.5	1

Table 1. *Cont.*

ICT Model		
Parameter	**Value**	**Units**
N_0	1.5×10^{19}	m^{-3}
ψ_{dis}	0.8	eV
δ_p	2.5×10^{-9}	m
δ_n	2×10^{-9}	m
w_{tp}	0.75	eV
w_{tn}	0.78	eV
B_p	0.18	s^{-1}
B_n	0.15	s^{-1}
ψ_{pt}	0.92	eV
ψ_{nt}	0.9	eV
n_{0pt}	100	C/m^3
n_{0nt}	100	C/m^3
ξ_0,ξ_1,ξ_2	4×10^{-3}	m^{-3} C/s
ζ_3	0	m^{-3} C/s

2.2. Geometric Model Used for Simulation

A one-dimensional axisymmetric geometric model used for the simulation is constructed on the basis of an actual 160 kV DC polymeric cable, as shown in Figure 2. The model is built by the 360-degree rotation of the segment O-G around the center O. In Figure 2, segment O-A is the conductor radius, segment O-B (r_{in}) is the outer radius of the conductor shield and the inner radius of the polymeric insulation layer, segment O-C (r_{out}) is the outer radius of the polymeric insulation layer, segment O-D is the outer radius of the insulation shield, segment O-E is the water blocking layer, segment O-F is the outer radius of the metal sheath, and segment O-G is the outer radius of the outer sheath. The selection of the structural dimensions and material properties in the geometric model are guided in [27–29], as listed in Table 2.

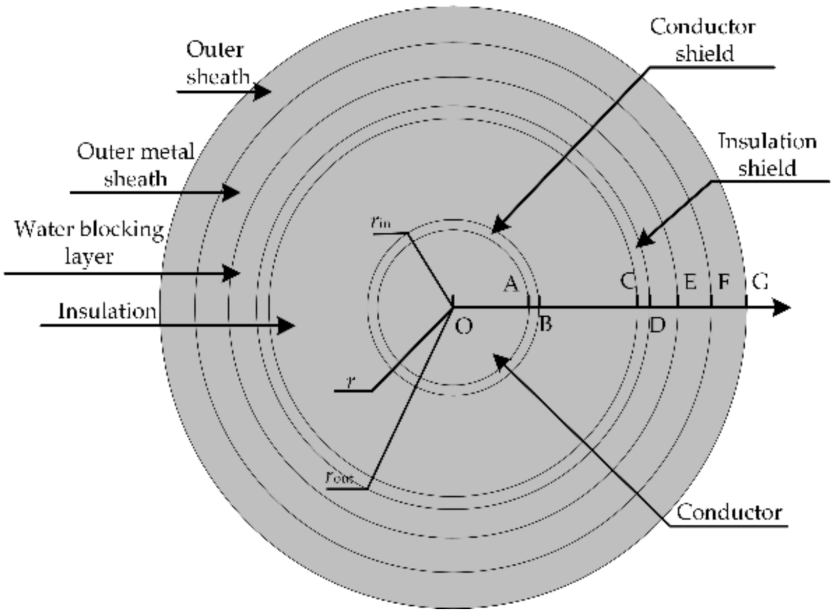

Figure 2. The simulated geometric model.

Table 2. Structural dimensions and material properties in the geometric model.

Structure	Radius /mm	Thermal Conductivity /Wm^{-1} K^{-1}	Heat Capacity /Jkg^{-1} K^{-1}	Density /kg^{-1} m^3
Conductor	12.62	400	390	8900
Conductor shield	14.12	0.29	1900	1100
Insulation	30.12	0.29	1900	930
Insulation shield	31.12	0.29	1900	1100
Water Blocking Layer	34.12	0.17	2200	350
Metal sheath	40.12	237	880	2700
Outer sheath	46.12	0.5	1900	950

The geometric model shown in Figure 2 is discretized using with a non-uniform grid of cells of thickness Δr. The time step Δt used for the simulation satisfied the Courant–Friedrichs–Lewy (CFL) condition [30], demonstrating that the charge transport distance within each time step Δt was less than the cell size Δr.

2.3. Initial Conditions and Boundary Conditions in the Improved Model

The initial temperature for the polymeric insulation is set to the ambient temperature (20 °C), while the initial charge density is set to 0 C/m^3. The detailed boundary conditions in the improved model are set as follows.

2.3.1. Electric Field

In order to realistically reflect the polarity reversal process in a practical HVDC transmission system, a time-varying DC voltage $U(t)$, shown in Figure 3, is applied to simulate the different stages, including before the VPR and after the VPR and during the VPR. In Figure 1, the $U(t)$ is applied to the conductor, and the outer sheath is grounded. As shown in Figure 3, the relevant voltage stages are summarized as follows:

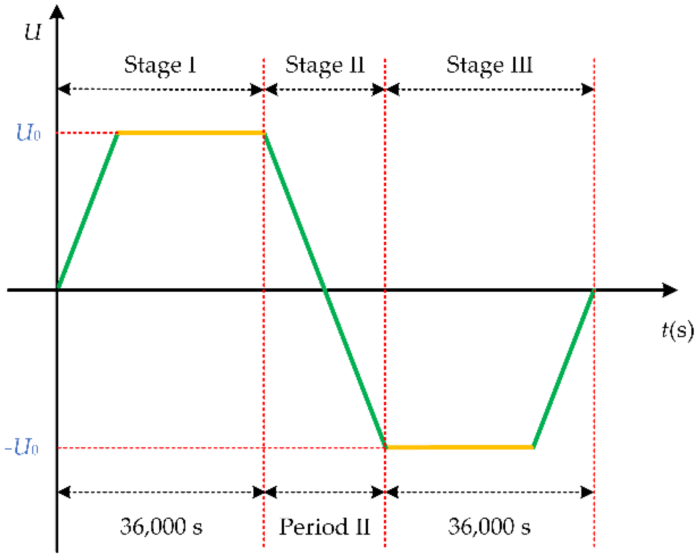

Figure 3. DC external voltage application procedure.

Stage I: The applied voltage $U(t)$ is raised to U_0 (320 kV). The reached final value U_0 then maintains a stable operation for 36,000 s. Stage II: during the VPR, the voltage polarity is reversed from U_0 (320 kV) to $-U_0$ (−320 kV). Stage III: after the VPR, the reached final value $-U_0$ (−320 kV) also maintains a stable operation for 36,000 s. $U(t)$ then decreased to 0.

2.3.2. Heat Transfer

The TG across the insulation formed by the load current originates from the heat transfer equations of time dependence along the radial direction:

$$\rho C_p \frac{\partial T(r,t)}{\partial t} - \nabla \cdot (\lambda \nabla T(r,t)) = Q \tag{15}$$

$$Q = \frac{W_c}{N} \tag{16}$$

where ρ denotes the insulating material density, C_p represents the constant pressure heat capacity, λ is the thermal conductivity, Q denotes the heat source originating from the Joule loss generated by the load current in the conductor, N is the cross section of the conductor, and W_c denotes the conductor loss per unit length, given by:

$$W_c = {I_L}^2 R_{DC} \tag{17}$$

$$R_{DC} = R_0 + R_0 \alpha_{20} (T_c - 20) \tag{18}$$

where I_L is the load current, R_{DC} represents the DC resistance per unit length of the conductor, R_0 denotes the DC resistance per unit length of the conductor at 20 °C (R_0 = 3.44 × 10^{-5} Ω/m), α_{20} is the temperature coefficient for the DC resistance of the conductor at 20 °C (α_{20} = 3.93 × 10^{-3}), and T_c is the operation temperature (T_c = 90 °C). Moreover, the convective heat flux q_0 is set to the boundary condition at the outer sheath, expressed as:

$$q_0 = h(T_{ext} - T(r,t)) \tag{19}$$

where h is the convective heat transfer coefficient and T_{ext} is the ambient temperature.

In the geometric model, the insulation thickness is set to 16 mm, while the cross section of the conductor is set to 500 mm^2. According to [29], the calculated maximum load current during the cable operation is equal to 1090 A. In order to obtain different TGs across the insulation, the load currents I_L are respectively set to 800 A and 1000 A. The time-varying temperatures in the conductor, inner insulation layer and outer insulation layer are shown in Figure 4. The figure shows that the temperatures at the previously mentioned layers reach a steady-state distribution after approximately 28,000 s.

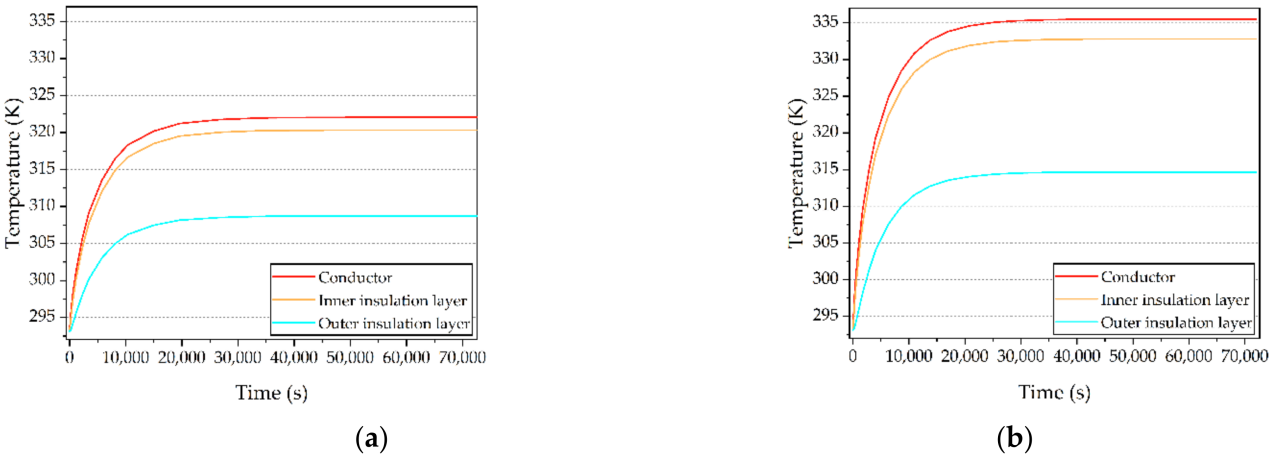

Figure 4. Time-varying temperatures in the conductor, inner insulation layer and outer insulation layer, with applied load currents: (**a**) 800 A; (**b**) 1000 A.

It can be seen from Figure 4a that the steady-state temperatures of the conductor, the inner insulation layer and the outer insulation layer are approximately 335.5 K, 332.8 K and 314.7 K, respectively, thereby forming the TG of about 1.1 K/mm across the insulation.

It can be observed in Figure 4b that the steady temperatures of the conductor, the inner insulation layer and the outer insulation layer are, respectively, 322.1 K, 320.3 K and 308.7 K, thereby forming the TG of about 0.7 K/mm across the polymeric insulation. The steady-state temperature distributions in the HVDC extruded cable are illustrated in Figure 5 with load currents of 800 A and 1000 A.

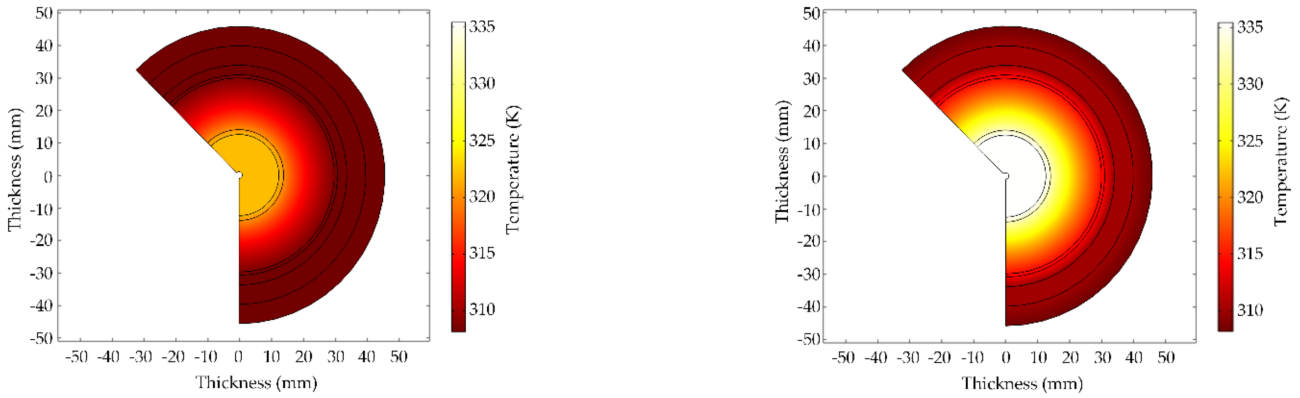

Figure 5. Steady-state temperature distribution in the HVDC extruded cable, with applied load currents: (**a**) 800 A; (**b**) 1000 A.

2.3.3. Space Charge Injection and Extraction

The threshold field value for charge injection in polyethylene is approximately 10 kV/mm [31,32]. Thus, the boundary conditions for the charge injection at both electrodes are defined by (1), when the field exceeding the threshold value is applied. On the basis of the low-field conduction mechanism [1], an Ohmic conduction exists at low field. Hence, during the applied field below the threshold value, we assume that the boundary conditions for the charge generation at both electrodes originate from the Ohmic conduction, defined by a first-order linear equation. Furthermore, the boundary conditions for charge extraction are defined by (7). The direction of the extraction current is chosen opposite to that of the applied field. The detailed conduction mechanism at the anode during the applied DC voltage in Figure 3 is illustrated in Figure 6, where it can be seen that the conduction mechanism transition from low field (Ohmic conduction) to high field (Schottky injection) is achieved at the threshold value (10 kV/mm). Figure 6a illustrates the conduction mechanism at the anode during Stage I, while Figure 6b presents the conduction mechanism during Stage II, and under the applied stable voltage $-U_0$ in Stage III.

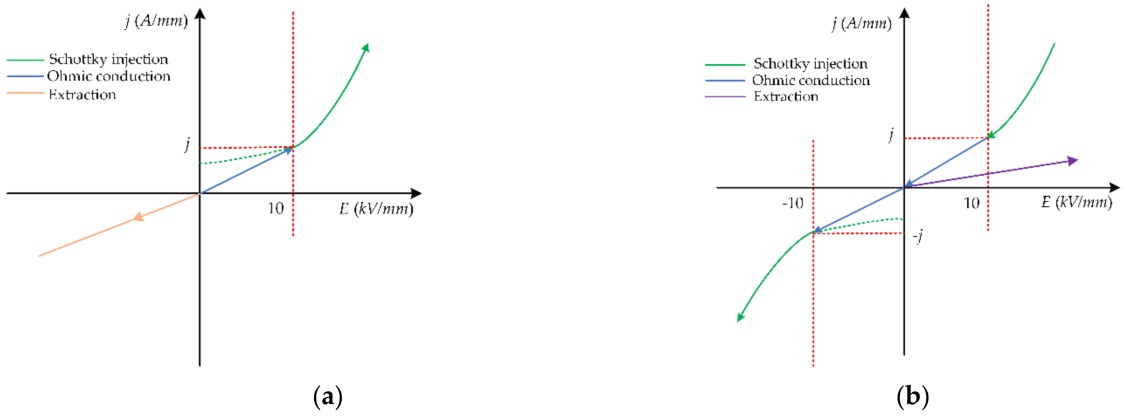

Figure 6. Conduction mechanism during the applied DC voltage shown in Figure 3 at the anode: (**a**) Stage I; (**b**) Stage II and the application of stable external voltage $-U_0$ in Stage III.

3. Simulation Result

3.1. Influence of the Polarity Reversal Period on the Space Charge Accumulation and the Electric Field Distribution

As mentioned in Section 1, the PRP in the model is set to 6 s, 30 s and 120 s, while the load current is set to 1000 A. Figure 7 presents the evolution of space charge in the cable insulation at a load current of 1000 A, under the applied DC voltage in Figure 3 with a PRP of 6 s, 30 s and 120 s. This depicts the charge evolution from a steady-state distribution before the VPR to a transient process during the PR, and then a new steady-state distribution after the VPR. In Figure 7, the horizontal axis represents the radial position of the insulation layer, the left vertical axis is the polarization time, and the right vertical axis denotes the charge density. The time scale ranges from 36,000 s to 70,000 s.

It can be seen from Figure 7a that, after reaching a steady-state charge distribution before the PR, the amount of injected charge at the interface between the conductor shield and the insulation is higher than that at the interface between the insulation and the insulation shield. A positive homocharge appears near the interface between the conductor shield and the insulation, while a positive heterocharge accumulates near the interface between the insulation and the insulation shield. This can reproduce the feature of the heterocharge accumulation experimentally observed in a 160 kV DC polymeric cable under TG [33]. Moreover, a few positive charges accumulate in the bulk insulation, which is mainly located in the middle part of the cable insulation.

During the VPR (ramping down of the applied positive voltage in Stage II), the amount of injected charge at both electrodes decreases. However, the positive homocharge still gradually accumulates in the vicinity of the interface between the conductor shield and the insulation. The amount of positive heterocharge in the vicinity of the interface between the insulation and the insulation shield slightly decreases, and there are still accumulated positive charges in the bulk insulation (cf. Figure 7a).

As illustrated in Figure 7a, just after the VPR is finished, the polarities of space charge do not rapidly change with the VPR, while the amount of injected charge from both electrodes decreases. During the initial period of Stage III, the amount of the residual positive heterocharge near the inner semicon–insulation interface and positive charge in the bulk insulation before the VPR are first decreased. The polarity of partial charges in the bulk insulation is then reversed. More precisely, it can be clearly seen that the successive positive and negative peaks appear in the bulk insulation. With the increase in the poling time after the VPR, the negative homocharge gradually appears near the inner semicon–insulation interface, while negative charges also extend into the bulk insulation. Moreover, the negative heterocharge gradually accumulates near the insulation–outer semicon interface. The region of heterocharge accumulation is almost the same as that of the positive heterocharge before the VPR. The steady-state charge distribution before and after the VPR presents almost symmetrical profiles, which is consistent with the description of the "mirror image effect" phenomenon [12].

A comparison between Figure 7a–c is performed, demonstrating that some specific features for the charge evolution during a PRP of 6 s and 30 s are similar to these during a PRP of 120 s. However, there are some differences reflected in the following description. (i) The variation of the charge evolution is not obvious during the VRP with a PRP of 6 s, while there is almost no change in the density of injected charges from both electrodes. (ii) During the initial period of Stage III, the longer the PRP, the more residual positive heterocharge accumulates adjacent to the interface between the conductor shield and the insulation, but the fewer the negative charges that extend into the bulk insulation.

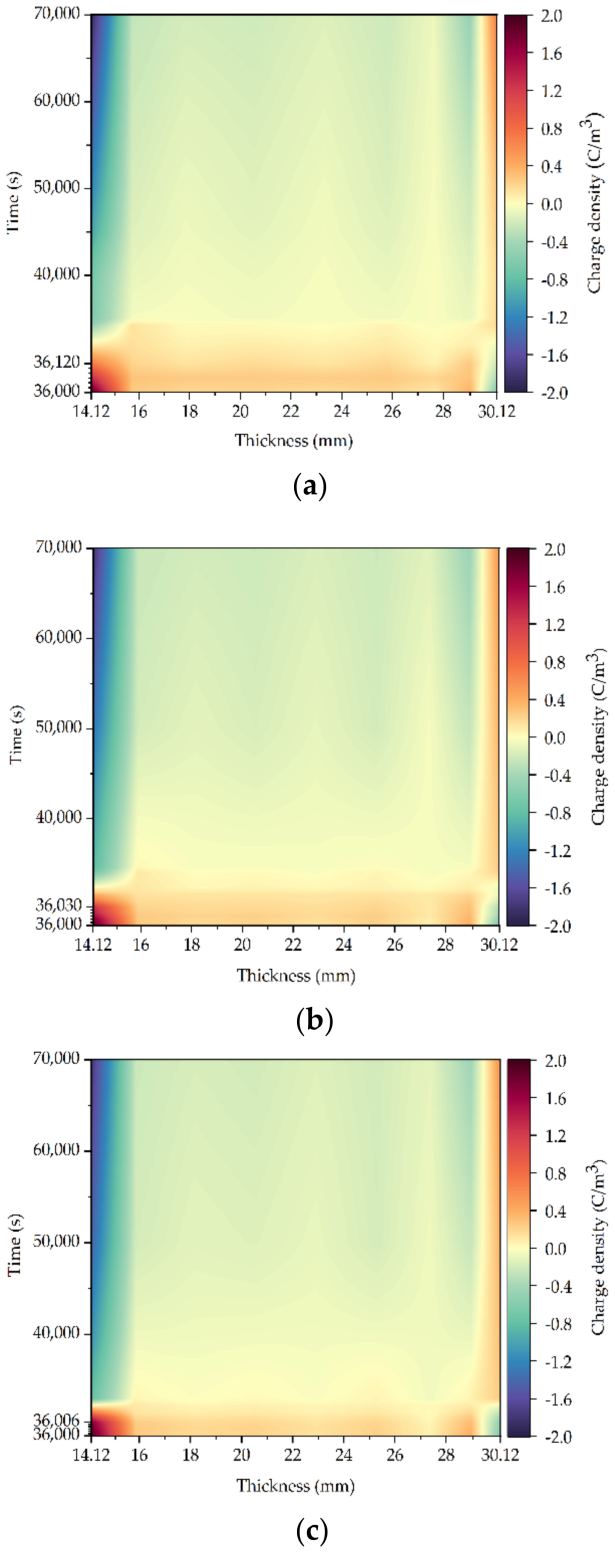

Figure 7. Space charge evolution in the HVDC extruded cable at load current of 1000 A, under the applied DC voltage shown in Figure 3 with different PRPs: (**a**) 120 s; (**b**) 30 s; (**c**) 6 s.

Figure 8a–c presents the electric field distribution in the cable insulation at a load current of 1000 A under the applied DC voltage in Figure 3, with a PRP of 120 s, 30 s and 6 s, respectively. In this figure, the horizontal axis is the radial position of the insulation

layer, the left vertical axis is the polarization time, and the right vertical axis is the field strength. The time scale ranges from 36,000 s to 70,000 s.

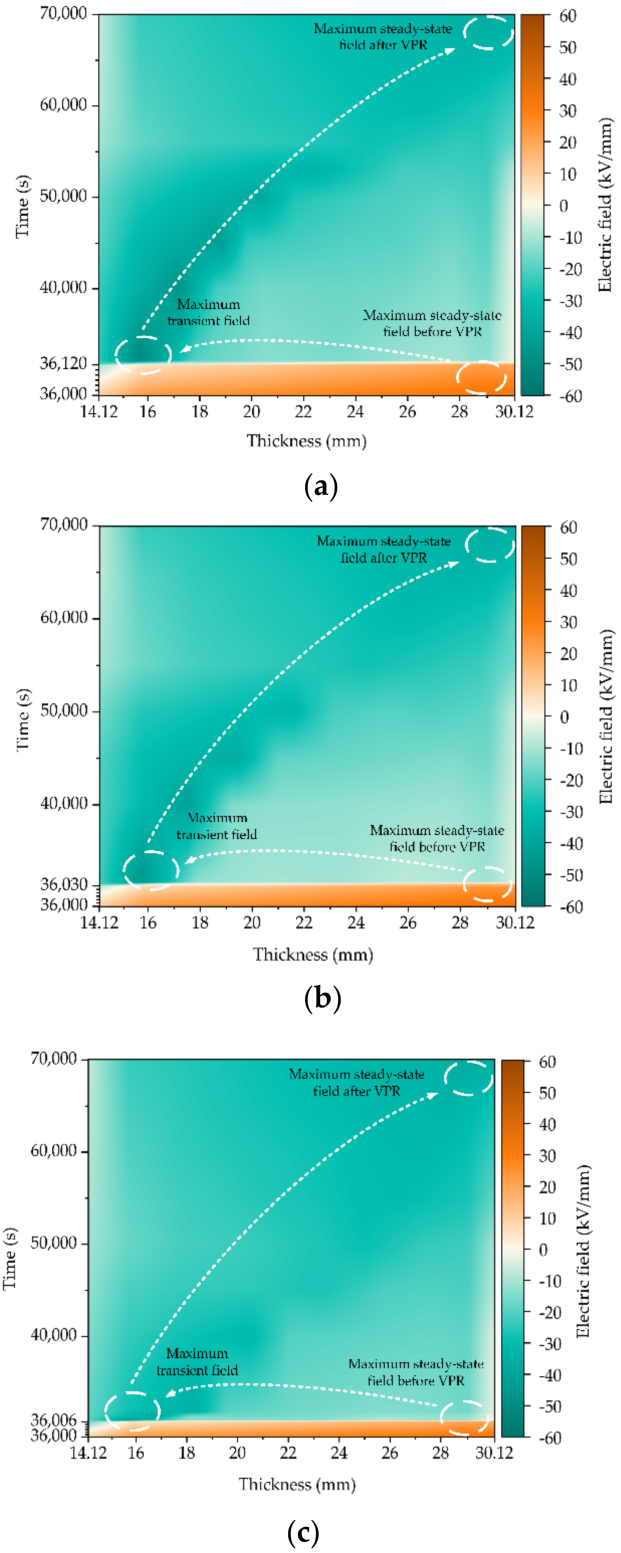

Figure 8. Space charge evolution in the HVDC extruded cable at a load current of 1000 A, under the applied DC voltage shown in Figure 3 with different PRPs: (**a**) 120 s; (**b**) 30 s; (**c**) 6 s.

It can be observed from Figure 8 that the variation trends for the maximum field location during the polarization under different PRPs are basically the same. The location of the maximum steady-state field appears near the interface between the insulation and the insulation shield just before the VPR, which is consistent with the location in the field inversion phenomenon experimentally observed in [34]. During the initial period of Stage III, the location of the maximum transient field switches from the vicinity of the insulation–outer semicon interface to the vicinity of the inner semicon–insulation interface. After reaching a steady-state field distribution in Stage III, the location of the maximum field reverses again and returns to the location near the interface between the insulation and the insulation shield. Therefore, an almost symmetrical field distribution is formed compared with that before the VPR. In addition, the decrease in the PRP shortens the time required to reach the maximum transient field.

Moreover, the absolute values of the maximum transient fields and the corresponding field distortion rates under a PRP of 6 s, 30 s, and 120 s are evaluated on the basis of (20) [8], and they are illustrated in Figure 9. Furthermore, the line graph in Figure 9 illustrates the variations of the maximum transient fields under the corresponding PRPs.

$$F = \frac{|E_{\max}| - |E_{\text{ave}}|}{|E_{\text{ave}}|} \times 100\% \tag{20}$$

where F is the field distortion rate and E_{ave} is the applied field average value.

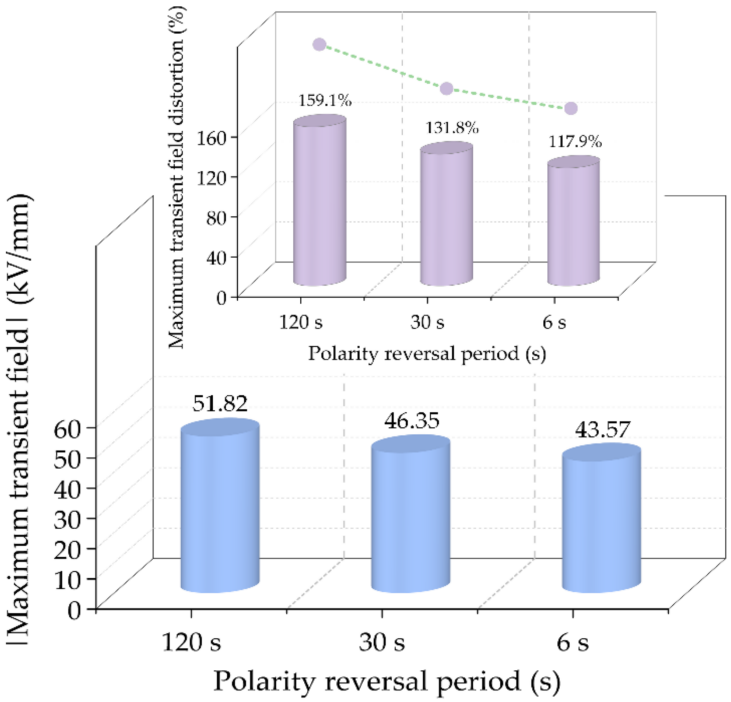

Figure 9. Absolute values of maximum transient fields and the corresponding field distortion, under a PRP of 120 s, 30 s and 6 s.

It can be seen from Figure 9 that during the initial period of Stage III, the longer the PRP the higher the maximum transient field strength near the interface between the conductor shield and the insulation, and the more serious the field distortion.

3.2. Influence of the Temperature Gradient on the Space Charge Accumulation and the Electric Field Distribution

Figure 10 illustrates the evolution of space charge in the cable insulation at a load current of 800 A, under the applied DC voltage in Figure 3 with a PRP of 120 s.

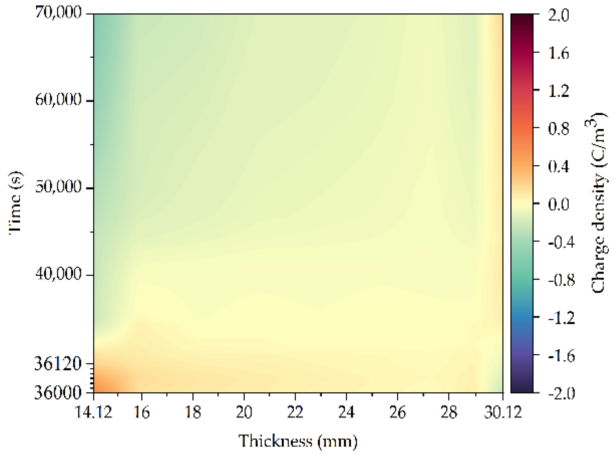

Figure 10. Space charge evolution in the HVDC extruded cable at a load current of 800 A, under the applied DC voltage shown in Figure 3 with a PRP of 120 s.

By comparing Figure 7a with Figure 10, it can be concluded that the overall characteristic features of space charge evolution shown in Figure 7a are reproduced in Figure 10. However, some differences remain, as expressed in the following. (i) When the distribution of space charge has reached a steady state before the VPR, the higher the load current (1000 A), the more positive homocharge remains near the interface between the conductor shield and the insulation, and the deeper the range of positive charge penetrates into the bulk insulation. Moreover, a higher TG leads to more positive heterocharge accumulating near the interface between the insulation and the insulation shield. (ii) During the initial period of Stage III, under the action of higher load current, more charges are injected from both electrodes, and more positive previously accumulated heterocharge remain near the interface between the conductor shield and the insulation. (iii) After the VPR in Stage III, the influence of the higher TG on the steady-state charge distribution is almost the same as that before the PR described in Section 1, in spite of the opposite polarity for the corresponding charges.

Figure 11 shows the electric field distribution in the cable insulation at a load current of 800 A, under the applied voltage in Figure 3 with a PRP of 120 s. It can be observed that the maximum field appears in the bulk insulation just before the VPR, which is located on the right side of the middle part of the bulk insulation. By comparison with Figure 8a, it can be deduced that the TG enhancement promotes the location of the maximum field to move towards the insulation–outer semicon interface. During the initial period of Stage III, the location of the maximum transient field shifts from the bulk insulation to the location near the interface between the conductor shield and the insulation, which is almost the same as that obtained with a load current of 1000 A (cf. Figure 8a). After reaching the steady-state field distribution in Stage III, the maximum field location shifts from the vicinity of the inner semicon–insulation interface to the right side of the middle part of the bulk insulation, forming an almost symmetrical field distribution compared with that before the VPR.

Furthermore, according to Equation (20), the absolute values of the maximum transient fields and their distortion rates at a load current of 800 A with a PRP of 120 s under steady and transient states are shown in Figure 12. The corresponding field distortion rates at a load current of 1000 A are also presented in Figure 12 for a clear visual comparison. It is demonstrated in Figure 12 that the higher TG intensifies the maximum fields under steady and transient states, leading to more serious field distortion.

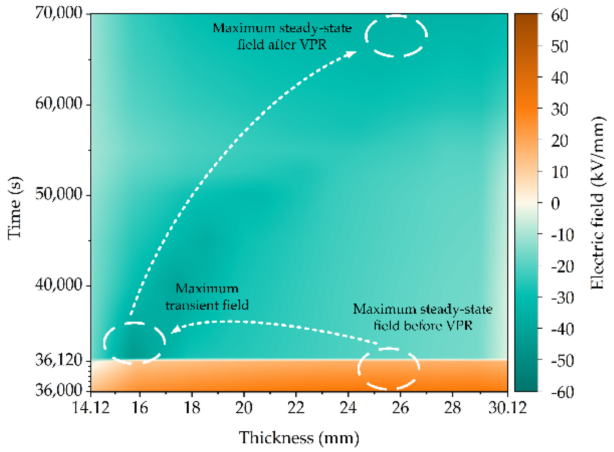

Figure 11. Electric field distribution in the HVDC extruded cable at a load current of 800 A, under the applied DC voltage shown in Figure 3 with a PRP of 120 s.

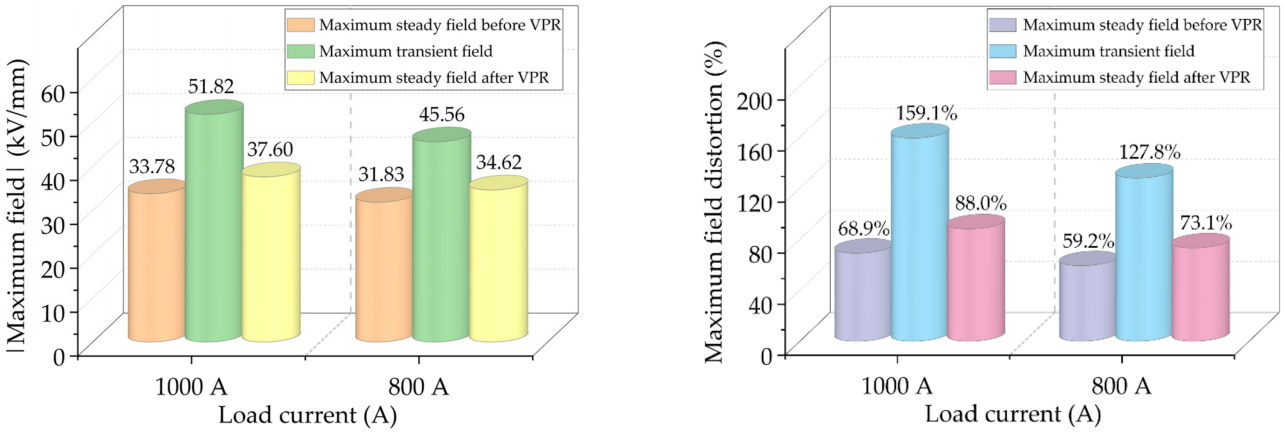

Figure 12. Absolute values of maximum transient fields and the corresponding field distortion with a PRP of 120 s, under steady and transient states: (**a**) Maximum field; (**b**) Maximum field distortion.

4. Discusion

4.1. Mechanism of Space Charge Dynamics under Different Polarity Reversal Periods

As previously seen in Figure 7, on the basis of the improved charge transport model, the homocharge region mainly originates from the trapping of the injected carriers at each electrode, which is considered as the extension of the injected carriers into the bulk insulation. The heterocharge is generated by the ionization of impurities and the blocked extraction of injected carriers. The mechanism models of space charge generation and transport in HVDC extruded cable under VPR are illustrated schematically in Figure 13. The relevant mechanisms showing the influence of the PRP on the charge dynamics and the field distortion are elucidated in the following.

It has been reported in [8,35] that the mobility of holes is lower than that of electrons in polymeric insulation. During the VPR (ramping down of the applied voltage in Stage II), with the increase in the PRP, as the distance between the heterocharge region and the cathode is short, more positive heterocharge is extracted and neutralized by the injected electrodes from the cathode. This results in a smaller amount of positive heterocharge remaining in the vicinity of the interface between the insulation and the insulation shield. On the other hand, more electrons from the cathode move towards the bulk insulation owing to higher mobility of electrons. The longer the PRP, the more the electron–hole recombination, the more the negative ions–positive ions recombination, and the fewer

positive charges accumulated in the bulk insulation. Moreover, during the period, the longer PRP contributes to more injected holes trapped near the interface between the conductor shield and the insulation, the longer PRP provides more ionic carriers generated by impurity dissociation. However, due to the relatively short PRP and the thick polymeric insulation for HVDC extruded cable, the negative ions and the electrons from the counter electrode are not easily moved to the anode. This leads to a weak neutralization on the homocharge accumulation. Hence, during the period, the longer the PRP, the more positive homocharge accumulates near the interface between the conductor shield and insulation (see Figure 7).

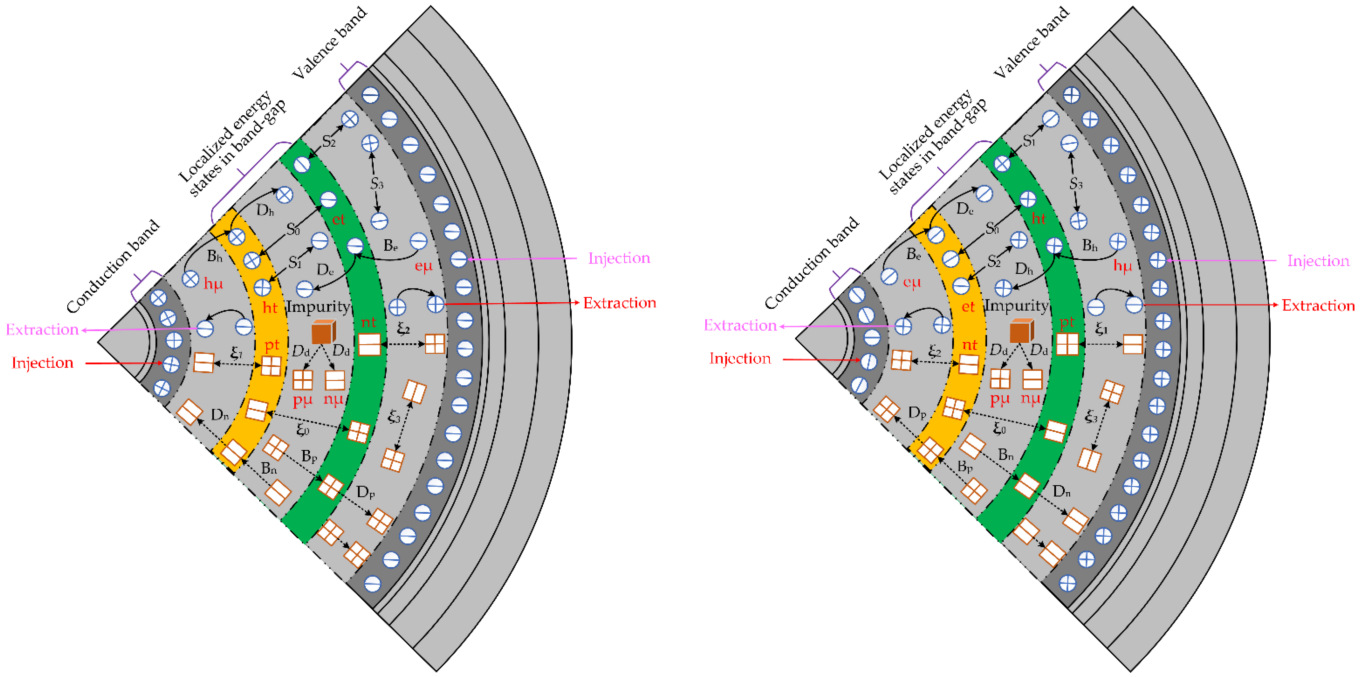

Figure 13. Mechanism model of space charge generation and transport in the HVDC extruded cable under VPR: (**a**) Before the VPR; (**b**) After the VPR.

During the VPR (ramping up of the applied negative voltage in Stage II), due to the relatively short PRP and the thick polymeric insulation for the HVDC extruded cable, the injected carriers with reversed polarity have a weaker neutralization effect on the remaining charges in the corresponding locations before the VPR (e.g., positive homocharge). Therefore, the charge polarity cannot keep up with the change of voltage polarity at the moment when the VPR has just been completed, as shown in Figure 7. During the initial period of Stage III, when the charge polarity at each electrode has been reversed, the residual homocharge before the VPR acts as the heterocharge adjacent to the inner semicon–insulation interface. On the other hand, the heterocharge accumulated before the VPR acts as the homocharge adjacent to the insulation–outer semicon interface. This intensifies the field strength adjacent to the inner semicon–insulation interface, and alleviates the field strength adjacent to the insulation–outer semicon interface. Therefore, the location of the maximum field shifts from the vicinity of the insulation–outer semicon interface to the vicinity of the inner semicon–insulation interface (see Figure 8). During the period, the shorter PRP accelerates the charge injection under the action of $-U_0$; therefore, more positive homocharge accumulated before the VPR is extracted and neutralized by the injected carriers. Hence, during the initial period of Stage III, the longer the PRP, the more positive heterocharge remains in the vicinity of the inner semicon–insulation interface, resulting in a higher maximum transient field and more serious field distortion (cf. Figures 7 and 9).

As previously mentioned, after the VPR in Stage III, more injected electrons due to the shorter PRP contribute to the accumulation of negative homocharge adjacent to the inner semicon–insulation interface and negative charges in the bulk insulation, and this is done more quickly. In addition, because the injection of electrons is stronger than that of the holes under TG, and the mobility of holes is slower than that of electrons, more electrons are transported towards the counter electrode. In addition, the imbalance of electrons and holes can weaken the recombination effect, resulting in more electrons dominating the bulk insulation. The dominant electrons are extracted from the low-temperature electrode, and the rate of charge extraction at a low-temperature electrode is lower than that at high-temperature electrode under the TG, which causes the accumulation of a part of electrons in the vicinity of the insulation–outer semicon interface, owing to the blocked extraction. Moreover, more negative ions generated by the impurity dissociation in the bulk insulation move to the interface between the insulation and the insulation shield. Hence, after reaching a steady-state charge distribution, a large amount of negative heterocharge accumulates in the vicinity of the insulation–outer semicon interface, owing to the blocked extraction of electrons and the accumulation of negative ions. This results in intensifying the field distortion adjacent to the insulation–outer semicon interface; therefore, the location of the maximum field reverses again and returns to the vicinity of the insulation–outer semicon interface (cf. Figures 8 and 9).

4.2. Mechanism of Space Charge Dynamics under Different Temperature Gradients

On the basis of the mechanism model shown in Figure 13, the relevant mechanisms of the TG effect on the charge dynamics and the field distortion are clarified as follows.

By comparing Figure 7a with Figure 10, it can be deduced that before the VPR, the higher TG formed by the load current of 1000 A diminishes the injection barriers and intensifies the injected carriers at each electrode. The trapping of more injected holes forms a deeper range of homocharge region adjacent to the inner semicon–insulation interface. The de-trapping of trapped carriers is also enhanced, and the mobile carriers of a higher mobility then extend into the bulk insulation. On the other hand, the higher TG aggravates the concentration imbalance between holes and electrons, resulting in more positive charges dominating the bulk insulation. In addition, the higher the TG, the more heterocharge accumulates in the vicinity of the insulation–outer semicon interface. As described in Section 4.1, the ionization of impurities and the blocked extraction of injected carriers in the improved model contribute to the heterocharge accumulation. Hence, the higher levels of heterocharge accumulation adjacent to the insulation–outer semicon interface under the higher TG may originate for the following reasons. (i) The higher TG intensifies the impurities dissociation, leading to the generation of more ionic carriers, and more positive ions with a faster mobility move towards the low-temperature electrode. This results in greater heterocharge remaining in the vicinity of the insulation–outer semicon interface. (ii) The dominant holes are extracted from the cathode. Due to the lower rate of charge extraction at the low-temperature electrode, not all the mobile holes are completely extracted. The higher the TG, the greater the gap between the injection rate and the extraction rate, and the extraction pressure of the holes from the cathode is intensified. Thus, more heterocharge accumulates in the vicinity of the insulation–outer semicon interface. Moreover, owing to the accumulation of more heterocharge adjacent to the insulation–outer semicon interface, the higher the TG, the more serious the maximum steady-state field distortion at the end of Stage I (cf. Figures 7a, 10 and 12).

During the initial period of Stage III, under the higher TG, the electron injection at the cathode and the de-trapping of trapped electrons are intensified. More positive heterocharge at the high-temperature electrode is extracted and neutralized by the injected electrons. However, due to the accumulation of more positive homocharge before the VPR under the higher TG, more positive heterocharge remains in the vicinity of the inner semicon–insulation interface. This leads to the higher maximum transient field and the more serious field distortion (see Figure 12).

During the polarization in Stage III, the higher levels of injected electrons due to the higher TG contribute to faster accumulation of negative homocharge near the inner semicon–insulation interface and negative charges in the bulk insulation. Except for the opposite polarity for the corresponding carriers, the discussion of the TG's influences on the charge dynamics after the VPR also applies for that before the VPR, detailed in this section. The higher TG enhances the impurity dissociation and the blocked extraction of electrons. This leads to the accumulation of more negative heterocharge adjacent to the insulation–outer semicon interface, and the more serious maximum steady-state field distortion (cf. Figures 8a, 11 and 12).

5. Conclusions

In this paper, a BCT model developed for cylindrical geometry is improved by introducing ionic carriers from impurity dissociation for the simulation of space charge and electric field in a 160 kV DC polymeric cable under VPR. The influence of PRP and TG on space charge evolution and electric field distribution is analyzed. The mechanisms of the charge dynamics and the field distortion affected by the PRP and the TG are elucidated. The conclusions can be summarized as follows:

(1) The improved model can be employed to simulate the space charge evolution and the electric field distribution in an HVDC extruded cable with thick polymeric insulation under complex operating conditions of electro-thermal (DC field, PR field, and TG) multi-field coupling. The improved model can effectively predict the heterocharge accumulation in the HVDC extruded cable, and assist in evaluating the ability of the insulating material to resist PR field. The research provides theoretical support for the precise regulation of space charge accumulation, the development of new insulating materials, and optimum design for HVDC extruded cable.

(2) In an HVDC extruded cable with thick polymeric insulation, the maximum transient field appears near the interface between the conductor shield and the insulation in the early stage of complete VPR. This demonstrates that the polymeric insulation breakdown for HVDC extruded cable may easily occur in the early stage of complete VPR. The reason for the distortion of the maximum transient field is the heterocharge accumulation in the vicinity of the interface between the conductor shield and the insulation. Hence, more attention should be paid to the semi-conductive shield layers in the HVDC extruded cable. In future work, the semi-conductive shield layers can be improved in the modification of semi-conductive materials (e.g., nanoparticle doping), the semicon–insulation interface matching, and the manufacturing technology, in order to evaluate the suppression of space charge injection and accumulation.

(3) Under the action of a load current flowing through the conductor, the longer the PRP, the higher the maximum transient field near the interface between the conductor shield and the insulation, and the more serious the maximum transient field distortion. Moreover, the decrease in PRP shortens the time required to reach the maximum transient field.

(4) The higher TG formed by a higher load current intensifies the maximum transient field near the interface between the conductor shield and the insulation. Consequently, a more serious distortion of the maximum transient field occurs. In addition, the higher TG also causes more serious distortion of the maximum steady-state field, before and after the VPR.

Author Contributions: Conceptualization, Y.Z. and W.W.; methodology, Y.Z. and W.W.; software, Y.Z., B.G. and K.S.; validation, Y.Z. and W.W.; formal analysis, Y.Z.; investigation, Y.Z. and B.G.; data curation, Y.Z. and B.G.; writing—original draft preparation, Y.Z.; writing—review and editing, Y.Z. and W.W.; visualization, Y.Z., B.G. and K.S.; supervision, W.W.; project administration, W.W.; funding acquisition, W.W. All authors have read and agreed to the published version of the manuscript.

Funding: This research was funded by the National Natural Science Foundation of China (Grant No. 51377056).

Conflicts of Interest: The authors declare no conflict of interest.

References

1. Mazzanti, G.; Marzinotto, M. *Extruded Cables for High Voltage Direct Current Transmission: Advances in Research and Development*; John Wiley & Sons: Hoboken, NJ, USA, 2013.
2. Albertini, M.; Bononi, S.F.; Giannini, S.; Mazzanti, G.; Guerrini, N. Testing challenges in the development of innovative ex-truded insulation for HVDC Cables. *IEEE Electr. Insul. Mag.* **2021**, *37*, 21–32. [CrossRef]
3. Su, R.; Wu, K.; Cheng, C.; Wu, Y.; He, Y.; Lv, Z.; Dissado, L.A. Carrier transport in LDPE and its nanocomposites. *IEEE Trans. Dielectr. Electr. Insul.* **2020**, *27*, 368–376. [CrossRef]
4. Baferani, M.A.; Li, C.; Shahsavarian, T.; Ronzello, J.; Cao, Y. High Temperature Insulation Materials for DC Cable Insulation—Part I: Space Charge and Conduction. *IEEE Trans. Dielectr. Electr. Insul.* **2021**, *28*, 223–230. [CrossRef]
5. Meng, F.-B.; Chen, X.; Dai, C.; Zhang, M.; Paramane, A.; Zheng, L.; Tanaka, Y. Effect of Thermal Ageing on Physico-Chemical and Electrical Properties of EHVDC XLPE Cable Insulation. *IEEE Trans. Dielectr. Electr. Insul.* **2021**, *28*, 1012–1019. [CrossRef]
6. TB 496. *Recommendations for Testing DC Extruded Cable Systems for Power Transmission at a Rated Voltage up to 500 kV*; CIGRE: Paris, France, 2012.
7. Li, G.; An, T.; Liang, J.; Liu, W.; Joseph, T.; Lu, J.; Szechtnman, M.; Andersen, B.R.; Lan, Y. Power reversal strategies for hybrid LCC/MMC HVDC systems. *CSEE J. Power Energy Syst.* **2020**, *6*, 203–212.
8. Chen, X.; Wang, X.; Wu, K.; Peng, Z.R.; Cheng, Y.H.; Tu, D.M. Effect of voltage reversal on space charge and transient field in LDPE films under temperature gradient. *IEEE Trans. Dielectr. Electr. Insul.* **2012**, *19*, 140–149. [CrossRef]
9. Wang, S.; Luo, S.; Tu, Y.; Wang, C.; Qin, S. Effect of polarity reversal on space charge properties of CB/LDPE composite under DC field. *IEEE Trans. Dielectr. Electr. Insul.* **2017**, *24*, 1349–1354. [CrossRef]
10. Tanaka, Y.; Fujitomi, T.; Kato, T.; Miyake, H.; Mori, H.; Kikuchi, S.; Yagi, Y. Packet-like charge formation in cable insulating materials at polarity reversal. *IEEE Trans. Dielectr. Electr. Insul.* **2017**, *24*, 1372–1379. [CrossRef]
11. Han, C.; Du, B.; Li, J.; Li, Z.; Tanaka, T. Investigation of charge transport and breakdown properties in XLPE/GO nanocom-posites part 2: Effect of polarity reversal. *IEEE Trans. Dielectr. Electr. Insul.* **2020**, *27*, 1213–1221. [CrossRef]
12. Fu, M.; Dissado, L.A.; Chen, G.; Fothergill, J.C. Space charge formation and its modified electric field under applied voltage reversal and temperature gradient in XLPE cable. *IEEE Trans. Dielectr. Electr. Insul.* **2008**, *15*, 851–860. [CrossRef]
13. Alison, J.M.; Hill, R.M. A model for bipolar charge transport, trapping and recombination in degassed crosslinked polyethene. *J. Phys. D Appl. Phys.* **1994**, *27*, 1291–1299. [CrossRef]
14. Le Roy, S.; Teyssedre, G.; Laurent, C. Modelling space charge in a cable geometry. *IEEE Trans. Dielectr. Electr. Insul.* **2016**, *23*, 2361–2367. [CrossRef]
15. Zhan, Y.; Chen, G.; Hao, M. Space charge modelling in HVDC extruded cable insulation. *IEEE Trans. Dielectr. Electr. Insul.* **2019**, *26*, 43–50. [CrossRef]
16. Boudou, L.; Griseri, V.; Guastavino, J.; Dissado, L.A. Effect of temperature on space charge formation in low density polyeth-ylene—Role of antioxidant. In Proceedings of the 2004 IEEE International Conference on Solid Dielectrics, Toulouse, France, 5–9 July 2004; pp. 252–255.
17. Mazzanti, G. Issues and Challenges for HVDC Extruded Cable Systems. *Energies* **2021**, *14*, 4504. [CrossRef]
18. Hozumi, N.; Takeda, T.; Suzuki, H.; Okamoto, T. Space charge behavior in XLPE cable insulation under 0.2-1.2 MV/cm dc fields. *IEEE Trans. Dielectr. Electr. Insul.* **1998**, *5*, 82–90. [CrossRef]
19. Fu, M.; Chen, G.; Dissado, L.; Fothergill, J. Influence of thermal treatment and residues on space charge accumulation in XLPE for DC power cable application. *IEEE Trans. Dielectr. Electr. Insul.* **2007**, *14*, 53–64. [CrossRef]
20. Hussin, N.; Chen, G. Analysis of space charge formation in LDPE in the presence of crosslinking byproducts. *IEEE Trans. Dielectr. Electr. Insul.* **2012**, *19*, 126–133. [CrossRef]
21. Su, R.; Wu, K.; Dissado, L.A.; Cheng, C.; Dodd, S.J.; Lv, Z.; Zhong, L.; Wang, X. Investigation of effects of charge injection and intrinsic ionic carriers in low-density polyethylene and cross-linked polyethylene. *J. Appl. Phys.* **2020**, *127*, 165103. [CrossRef]
22. Zhang, H.; Chen, M.; Wang, Y.; Wu, J.; Yin, Y. Interaction Effects of Three Major Crosslinking Byproducts on Space Charge Accumulation in Polyethylene. *IEEE Trans. Dielectr. Electr. Insul.* **2021**, *28*, 710–718. [CrossRef]
23. Boufayed, F.; Teyssèdre, G.; Laurent, C.; Le Roy, S.; Dissado, L.A.; Ségur, P.; Montanari, G.C. Models of bipolar charge transport in polyethylene. *J. Appl. Phys.* **2006**, *100*, 104105. [CrossRef]
24. Baudoin, F.; Le Roy, S.; Teyssedre, G.; Laurent, C. Bipolar charge transport model with trapping and recombination: An analysis of the current versus applied electric field characteristic in steady state conditions. *J. Phys. D Appl. Phys.* **2007**, *41*, 025306. [CrossRef]
25. Dissado, L.A. The role of theory of understanding space charge distributions. In Proceedings of the 2020 International Sym-posium on Electrical Insulating Material, Tokyo, Japan, 13–17 September 2020; pp. 1–14.
26. Lan, L. Effect of Temperature on Space Charge Distribution in Polymer Insulation. Ph.D. Thesis, Shanghai Jiao Tong University, Shanghai, China, 2015.
27. *IEC 60287-1-1.* Electric Cables—Calculation of the Current rating—Part 1-1: Current Rating Equations (100 % Load Factor) and Calculation of Losses. IEC: Geneva, Switzerland, 2006.
28. *IEC 60287-2-1.* Electric Cables—Calculation of the Current Rating—Part 2-1: Thermal Resistance—Calculation of Thermal Resistance. IEC: Geneva, Switzerland, 2006.
29. Hao, Y.; Huang, J.; Yang, L.; Fu, M.; Zhou, R. Analytical calculation method of steady-state current capacity of HVDC cables. *Power Syst. Technol.* **2016**, *40*, 1283–1288.

30. Le Roy, S. Numerical methods in the simulation of charge transport in solid dielectrics. *IEEE Trans. Dielectr. Electr. Insul.* **2006**, *13*, 239–246. [CrossRef]
31. Montanari, G.C.; Mazzanti, G.; Palmieri, F.; Motori, A.; Perego, G.; Serra, S. Space-charge trapping and conduction in LDPE, HDPE and XLPE. *J. Phys. D Appl. Phys.* **2001**, *34*, 2902–2911. [CrossRef]
32. Liu, N.; Zhou, C.; Chen, G.; Zhong, L. Determination of threshold electric field for charge injection in polymeric materials. *Appl. Phys. Lett.* **2015**, *106*, 192901. [CrossRef]
33. Wang, X.; Chen, C.; Cheng, C.; Wu, Y.; Wu, K.; Fu, M.; Hou, S.; Hui, B. Space charge characteristics in 160 kV DC XLPE cable under temperature gradient. *IEEE Trans. Dielectr. Electr. Insul.* **2018**, *25*, 2366–2374.
34. Fabiani, D.; Montanari, G.; Laurent, C.; Teyssedre, G.; Morshuis, P.; Bodega, R.; Dissado, L. HVDC Cable Design and Space Charge Accumulation. Part 3: Effect of Temperature Gradient [Feature article]. *IEEE Electr. Insul. Mag.* **2008**, *24*, 5–14. [CrossRef]
35. Chen, G.; Tay, T.Y.G.; Davies, A.E.; Tanaka, Y.; Takada, T. Electrodes and charge injection in low-density polyethylene using the pulsed electroacoustic technique. *IEEE Trans. Dielectr. Electr. Insul.* **2001**, *8*, 867–873. [CrossRef]